BIOCHEMISTRY
including biophysical chemistry & molecular biology

Article

pubs.acs.org/biochemistry

Methyl Relaxation Measurements Reveal Patterns of Fast Dynamics in a Viral RNA-Directed RNA Polymerase

Sébastien Alphonse,[†] Shibani Bhattacharya,[§] Hsin Wang,[†] and Ranajeet Ghose*[,†,‡]

[†]Department of Chemistry, The City College of New York, 160 Convent Avenue, New York, New York 10031, United States
[‡]Graduate Center of the City University of New York, 365 Fifth Avenue, New York, New York 10016, United States
[§]New York Structural Biology Center, 89 Convent Avenue, New York, New York 10027, United States

Supporting Information

ABSTRACT: Molecular dynamics (MD) simulations combined with biochemical studies have suggested the presence of long-range networks of functionally relevant conformational flexibility on the nanosecond time scale in single-subunit RNA polymerases in many RNA viruses. However, experimental verification of these dynamics at a sufficient level of detail has been lacking. Here we describe the fast, picosecond to nanosecond dynamics of an archetypal viral RNA-directed RNA polymerase (RdRp), the 75 kDa P2 protein from cystovirus ϕ12, using analyses of $^{1}H-^{1}H$ dipole−dipole cross-correlated relaxation at the methyl positions of Ile (δ1), Leu, Val, and Met residues. Our results, which represent the most detailed experimental characterization of fast dynamics in a viral RdRp until date, reveal a highly connected dynamic network as predicted by MD simulations of related systems. Our results suggest that the entry portals for template RNA and substrate NTPs are relatively disordered, while conserved motifs involved in metal binding, nucleotide selection, and catalysis display greater rigidity. Perturbations at the active site through metal binding or functional mutation affect dynamics not only in the immediate vicinity but also at remote regions. Comparison with the limited experimental and extensive functional and *in silico* results available for homologous systems suggests conservation of the overall pattern of dynamics in viral RdRps.

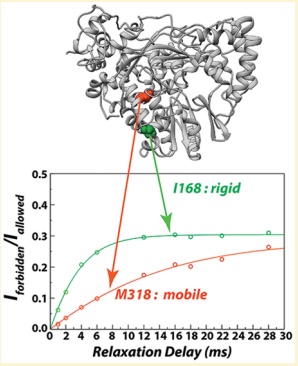

In RNA viruses, the production of viral proteins and recapitulation of the virus' genome within the host cell constitute two critical events necessary to propagate infection. These are mediated by two processes: transcription, the synthesis of plus-strand RNA to be utilized as mRNA by cellular ribosomes for viral protein translation; and replication, the synthesis of minus-strand RNA to recreate the genome in minus- or double-stranded RNA viruses or for use as templates to produce viral mRNA in plus-stranded RNA viruses. Both processes require the activity of a virus-encoded RNA-directed RNA polymerase (RdRp). While viral RdRps use distinct mechanisms to initiate RNA synthesis, with or without a short protein or nucleic acid primer (*de novo*), they share a similar overall fold (Figure 1A) resembling a cupped right hand with "thumb", "fingers", and "palm" domains.[1] In addition, viral RdRps contain conserved motifs [A−E in the palm domain and F in the fingers domain (Figure 1B)] that serve to bind RNA template (and primer, where applicable) and catalytic and structural divalent metal ions (Mg^{2+} and Mn^{2+}) and to stabilize the nascent daughter chain.

Viral RdRps utilize dynamics on multiple time scales to directly or indirectly modulate function[2] often with minimal perturbations in the static structures of their catalytic elements. Notably, remote events such as a mutation (G64S) in the poliovirus (PV) RdRp (3Dpol)[3] or the binding of an inhibitor on the thumb domain of the hepatitis C virus (HCV) RdRp (NS5B),[4] each occurring a considerable distance from the active site, leads to profound effects on the activities of the respective RdRps with minimal structural changes at the catalytic site. All-atom molecular dynamics (MD) simulations have suggested that the dynamics in both these specific cases show significant alterations with respect to those of the wild-type, resting enzymes.[5,6] Indeed, MD simulations on a range of viral RdRps[5−8] have provided tremendous insight into conformational dynamics not captured by crystal structures. These simulations have also revealed networks of residues that couple the dynamics of the catalytic site with those in remote regions.[9] However, the experimental determination of the dynamic landscape viral RdRps at a level of detail as fine as possible is critical to complement the *in silico* and the biochemical/functional data available for a wide range of viral RdRps. This understanding may help in the design of unique antiviral strategies that target the dynamics of remote sites that are dynamically coupled to the catalytic machinery[10] perhaps through the generation of mutator strains with increased fidelity reducing the relative population of drug-resistant variants, thus making the species more susceptible to targeted small molecule intervention.[3]

While solution nuclear magnetic resonance (NMR) seems to be the obvious choice for detailed analyses of viral RdRp

Received: July 22, 2015
Revised: September 1, 2015
Published: September 2, 2015

DOI: 10.1021/acs.biochem.5b00828
Biochemistry 2015, 54, 5828−5838

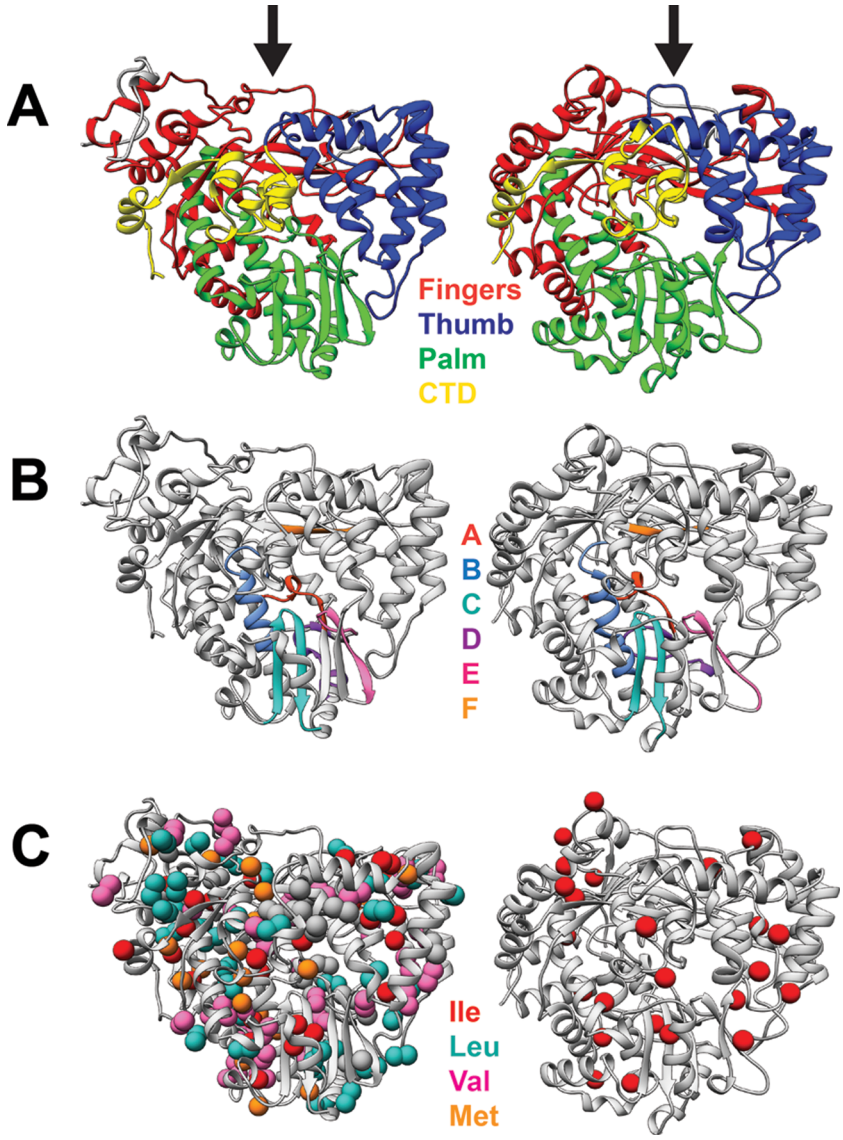

Figure 1. (A) Structural domains of the RdRps (P2) from cystoviruses ϕ12 (left) and ϕ6 (right). The domains are as follows: fingers (ϕ12, 35−78, 147−303, 358−420; ϕ6, 1−30, 104−276, 333−397; red), thumb (ϕ12, 82−134, 527−600; ϕ6, 37−91, 518−600; blue), palm (ϕ12, 304−357, 421−526; ϕ6, 277−332, 398−517), and the C-terminal domain (CTD; ϕ12, 601−659; ϕ6, 601−664; yellow). (B) Conserved sequence motifs A (ϕ12, 349−359; ϕ6, 324−334; orange-red), B (ϕ12, 416−436; ϕ6, 394−413; blue), C (ϕ12, 461−477; ϕ6, 445−461; coral green), D (ϕ12, 487−500; ϕ6, 475−488; purple), E (ϕ12, 505−517; ϕ6, 493−505; pink), and F (ϕ12, 295−299; ϕ6, 268−272; orange). (C) Methyl groups of Ile (δ1, both ϕ12 and ϕ6, red), Leu (ϕ12 only, coral green), Val (ϕ12 only, pink), and Met (ϕ12 only, orange) for which resonance assignments are available are shown on the three-dimensional structures of the cystoviral P2 proteins. Unassigned Ile (δ1 only), Leu, Val, and Met methyl groups are shown as gray spheres. The arrows in panel A denote the entrance to the template entry tunnel. The substrate NTPs enter through a tunnel at the back that is almost orthogonal to the template entry tunnel.

dynamics, this has been extremely challenging to date largely because of the large sizes of the viral RdRps (typically >50 kDa) and instability at the relatively high concentrations required for these studies. Nevertheless, NMR studies of viral RdRps are beginning to appear in the literature, including those that suggest dynamics on the catalytic microsecond to millisecond time scale.[11,12] However, these studies have relied on a very small number of probes of dynamics, e.g., 25 Ile δ1 positions in the RdRp (P2) from the cystovirus ϕ6[11,12] or 17 Met ε positions in PV 3Dpol.[13−15] As described recently,[16] we have obtained resonance assignments for a significantly larger number of methyl ^{13}C and ^{1}H resonances in the 75 kDa RdRp (P2) from cystovirus ϕ12, enhancing our ability to study the dynamics of a viral RdRp in a level of detail far greater than that previously possible. For ϕ12 P2, resonance assignments are now available for 31 of 32 Ile δ1 positions, 36 of 47 Leu δ positions, 37 of 44 Val γ positions, and 18 of 19 Met ε positions, providing ∼180 individual probes of structure and dynamics (Figure 1C). Using these resonance assignments and measurement of the intra-methyl ^{1}H−^{1}H dipole−dipole cross-correlation rate (η) that reports on the degree of order of the methyl rotation (C_3) axis,[17] we investigate the structural dynamics of ϕ12 P2 (termed P2 hereafter) on the fast, picosecond to nanosecond time scale. The significantly larger number of probes that are uniformly distributed over all the structural domains of P2 and cover all its sequence motifs provides the ability to analyze dynamics in a typical viral RdRp with a resolution far better than that previously possible. A

DOI: 10.1021/acs.biochem.5b00828
Biochemistry 2015, 54, 5828−5838

detailed analysis of these dynamics and its alteration upon binding divalent metals ions required for catalysis and substrate NTPs or in the presence of a functional mutation[18] suggests a network in which remote regions are dynamically coupled to the active site. Further, a reanalysis of the fast dynamics for the 25 Ile δ1 positions in the homologous ϕ6 P2 suggests that the overall patterns of dynamics are conserved in cystoviral RdRps and perhaps more widely.

MATERIALS AND METHODS

Sample Preparation. The cloning, expression, and purification of ϕ12 P2 have been described in detail previously[16] and will not be reproduced here. The *ts* mutant (T425I)[18] was expressed and purified in a fashion identical to that of wild-type P2. To obtain spectra of the highest quality possible for the cross-correlated relaxation measurements (described below) on ϕ12 P2 (and on the *ts* mutant), two separate samples, termed IM and LV, were used. The IM samples were labeled as follows: Ile ($^{13}CH_3$, δ1 only), Met ($^{13}CH_3$, the Met side chain was fully protonated), uniformly ^{2}H-labeled; LV samples were labeled as follows: Leu ($^{13}CH_3$, $^{12}CD_3$), Val ($^{13}CH_3$, $^{12}CD_3$), uniformly ^{2}H-labeled. P2 samples (~230 μM) were dissolved in a 100% D_2O-based buffer containing 20 mM Tris (pH 8), 150 mM NaCl, and 1 mM DTT. Additional experiments were performed on wild-type ϕ12 P2 in the presence of 5 mM $MgCl_2$ with and without 3 mM GMPCPP (Jena Bioscience GmbH).

Estimation of the Rotational Correlation Time and S_{axis}^2. The rotational diffusion tensor for ϕ12 P2 was calculated using the bead model as implemented in the HYDRONMR package.[19] The atomic radius, temperature, and viscosity were set to 3.2 Å, 298.15 K, and 1.089 cP, respectively. High-resolution crystal structures of P2 [Protein Data Bank (PDB) entries 4IEG and 4GZK][20] were utilized for the calculations. The radius of the solvent shell was automatically determined by the program.

The correlation times, τ_C, of wild-type P2 (also in the presence of Mg^{2+}) and the *ts* mutant were estimated using the one-dimensional (1D) ^{15}N, ^{1}H TRACT experiment[21] (at 600 MHz) that monitors the difference in the relaxation rates of the α state (R_α) and the β state (R_β) of the amide ^{15}N using relaxation delays of 0.11, 1.1, 3.23, 6.45, 9.68, 12.9, 19.35, 25.81, and 34.41 ms. The region between 8 and 10 ppm of the 1D spectra was integrated, and the integrated intensity as a function of the relaxation delay was fitted to a single-exponential decay separately for the α- and β-state spectra to obtain R_α and R_β values, respectively. The value of τ_C was obtained using a 1D grid search and the following equations:

$$R_\beta - R_\alpha = \frac{1}{6}\left(\frac{\mu_0}{4\pi}\right)\frac{\hbar\gamma_N{}^2\gamma_H B_0 \Delta\delta_N}{r_{NH}{}^3}(3\cos^2\theta - 1)\,[4J(0) + 3J(\omega_N)] \quad (1)$$

$$J(\omega) = \frac{2}{5}\frac{\tau_C}{1 + \omega^2\tau_C{}^2}$$

where r_{NH} = 1.02 Å, $\Delta\delta_N$ = 160 ppm, θ = 17°, and all other symbols have their usual meaning. The value of τ_C obtained in 10% D_2O was scaled to that in 100% D_2O using the linear dependence of the correlation time on viscosity in the Stokes–Einstein equation.

Measurement of Intra-Methyl Dipole–Dipole Cross-Correlation Rates. Experiments to determine the intra-methyl ^{1}H–^{1}H dipole–dipole cross-correlation rates[17] were performed at 25 °C with separate data sets being acquired for the "allowed" (64 scans per transient) and "forbidden" [64 scans per transient, except for T = 1 and 2 ms, where 128 scans were used (see below)] spectra. Measurements were performed on a 600 MHz Varian Inova spectrometer equipped with a triple-resonance cryogenic probe capable of applying pulsed field gradients along the *z*-axis. Experiments used sweep widths of 12 ppm (512 complex points) and 14 ppm (48 complex points) for the ^{1}H and ^{13}C dimensions, respectively, for the IM samples. For the LV sample, the corresponding values were 12 ppm (512 complex points) for the ^{1}H dimension and 11 ppm (48 complex points) for the ^{13}C dimension. Nine different values of the relaxation delay (T) of 1, 2, 4, 6, 12, 16, 18, 22, and 28 ms were used for the wild-type enzyme in absence or presence of Mg^{2+} and Mg^{2+}/GMPCPP. For the *ts* mutant, T values of 1, 2, 4, 6, 10, 14, 18, 22, and 26 ms were used. All relaxation data were processed using NMRpipe[22] and analyzed using NMRViewJ.[23] The intra-methyl ^{1}H–^{1}H dipole–dipole cross-correlation rates (η) were obtained by fitting the experimental data to eq 2 using in-house software that utilized the ODRPACK library.[24]

$$\frac{I_f}{I_a} = \frac{-0.5\eta\tanh(\sqrt{\eta^2 + \delta^2}\,T)}{\sqrt{\eta^2 + \delta^2} - \delta\tanh(\sqrt{\eta^2 + \delta^2}\,T)} \quad (2)$$

where I_a and I_f are intensities of corresponding peaks in the "allowed" and "forbidden" spectra, respectively, and δ is a leakage term due to ^{1}H–^{1}H cross-relaxation.[17] I_f values were appropriately scaled where necessary to account for the differences in the number of scans used in the "allowed" and "forbidden" spectra. The estimated cross-correlation rates were converted into the generalized order-parameter ($S_{axis}{}^2$) using

$$S_{axis}{}^2 = \frac{40}{9}\frac{r_{HH}{}^6}{\gamma_H{}^4\hbar^2\tau_C}\eta \quad (3)$$

where r_{HH} = 1.813 Å is the intra-methyl ^{1}H–^{1}H distance. All other terms have their usual meaning.

Chemical Shift Perturbations. Chemical shift perturbations were calculated using the following equation:

$$\Delta\delta = \sqrt{(\delta_{H,ref} - \delta_{H,i})^2 + \left[\frac{1}{3.94}(\delta_{C,ref} - \delta_{C,i})\right]^2} \quad (4)$$

where $\delta_{H,ref}$ ($\delta_{C,ref}$) and $\delta_{H,i}$ ($\delta_{C,i}$) are the methyl ^{1}H (^{13}C) chemical shifts in the reference state and in the liganded/mutated state, respectively. The factor of 3.94 represents the ratio of standard deviations of ^{1}H and ^{13}C chemical shifts averaged over the Ile, Leu, Val, and Met residues in the Biological Magnetic Resonance Data Bank. The unliganded protein was chosen as the reference state for determining the perturbations induced by the addition of Mg^{2+} ions or by mutations. The perturbations induced by Mg^{2+}/GMPCPP were calculated separately using either the apo state or the Mg^{2+}-bound state as reference.

Network Analysis. A T425I mutation was generated *in silico* using the "swapaa" command in UCSF Chimera[25] and the structures of ϕ12 P2 (PDB entries 4IEG and 4GZK).[20] Protons were added to the structures of both the wild type and the *in-silico* generated *ts* mutant that were subsequently minimized

DOI: 10.1021/acs.biochem.5b00828
Biochemistry 2015, 54, 5828–5838

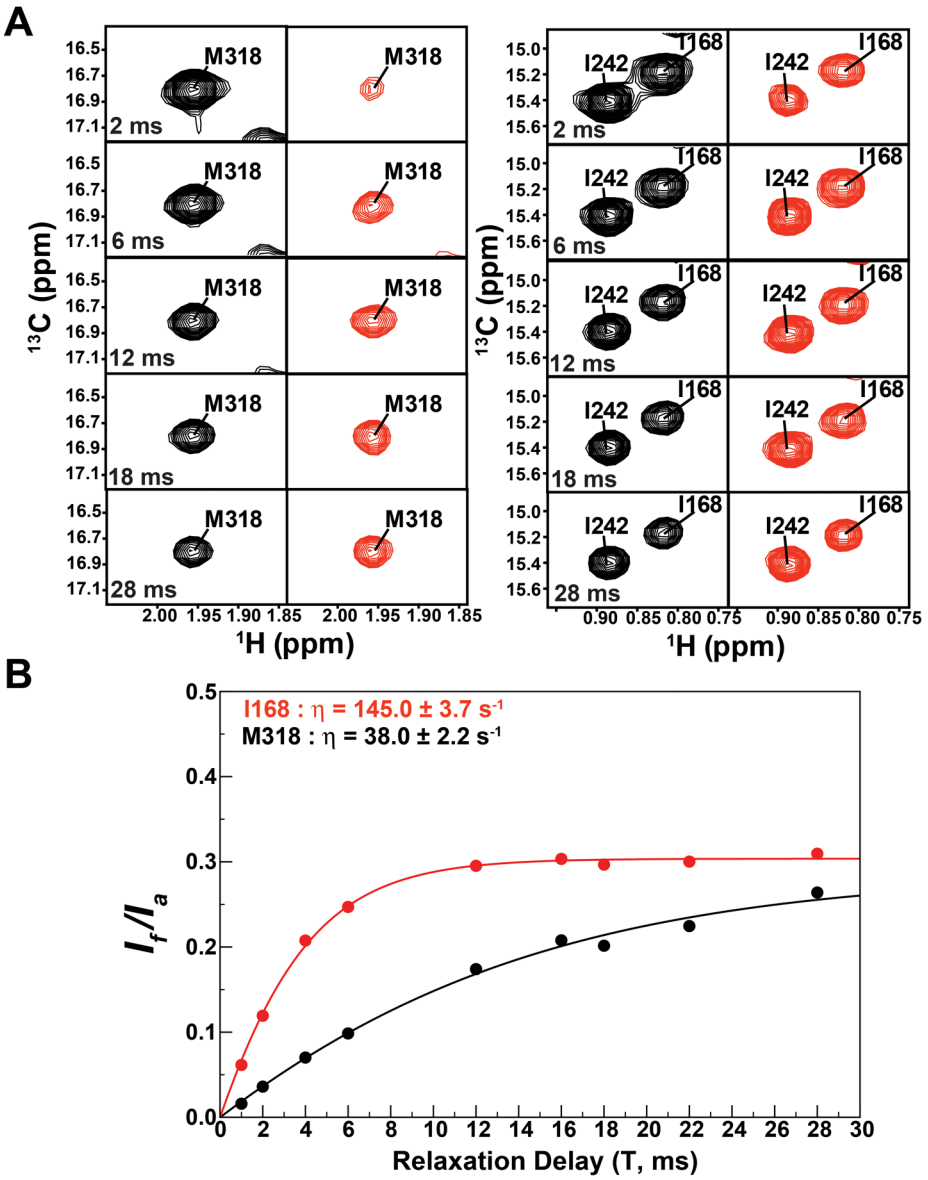

Figure 2. (A) Close-ups of the "allowed" (left) and "forbidden" spectra for M318 and I168 showing the change in peak intensities with relaxation delay (T). The "forbidden" spectra have been contoured at a level 3.8-fold lower than that of the "allowed" spectra. The forbidden spectrum for T = 1 ms uses double the number of scans as the corresponding allowed spectrum. (B) The experimental intensity ratios corresponding to the spectra shown in panel B (filled circles; black for M318 and red for I168) and the fits (solid lines) to eq 2 are shown.

using the AMBERff99SB force-field and standard protocols implemented in UCSF Chimera.[25] Network analysis was then performed on the minimized structures using the RINalyzer[26,27] plug-in for the Cytoscape (version 3.1.1) platform. Residue interaction networks (RINs) were generated from the static structures considering noncovalent interactions utilizing both backbone and side chain positions using default parameters. The shortest path closeness values for all nodes (residues) to residue 425 were computed using the number of interactions as the edge weight. Multiple edges were handled using a sum of weights. Scores were converted into distances using the |max-value| criterion. The cutoff for the weighted degree was set to 5. Shortest path closeness scores for Ile, Leu, Val, and Met residues were subsequently renormalized to obtain Π values using the following equation

$$\Pi = \frac{C_i}{C_{ILVM,max}} \quad (5)$$

where C_i is the closeness score for a particular Ile, Leu, Val, or Met residue and $C_{ILVM,max}$ is the maximal closeness score obtained for an Ile, Leu, Val, or Met residue. Thus, a Π of 1 implies that a particular residue has the highest closeness score among all Ile, Leu, Val, and Met residues in the structure.

RESULTS AND DISCUSSION

Measurement of Fast Dynamics of Methyl Groups. Given that for large proteins such as P2 conventional T_1, T_2, and {^{1}H}−^{15}N NOE-based approaches to determine the overall hydrodynamic properties[28] become inefficient, we pursued alternative strategies. Calculations using the available structures of P2[20] and the bead model as implemented in the HYDRONMR package[19] suggest a small degree of anisotropy

DOI: 10.1021/acs.biochem.5b00828
Biochemistry 2015, 54, 5828−5838

Table 1. S_{axis}^2 Values for Various Residue Types in ϕ12 P2

domain	residue	apo	Mg^{2+}	Mg^{2+}/GMPCPP	*ts* mutant
fingers	Ile	0.63 ± 0.27 (10)	0.67 ± 0.32 (10)	0.61 ± 0.27 (10)	0.66 ± 0.28 (10)
	Leu	0.69 ± 0.30 (22)	0.74 ± 0.29 (22)	0.69 ± 0.29 (21)	0.73 ± 0.32 (21)
	Val	0.71 ± 0.32 (20)	0.74 ± 0.33 (22)	0.66 ± 0.32 (19)	0.79 ± 0.31 (21)
	Met	0.31 ± 0.18 (6)	0.38 ± 0.23 (7)	0.36 ± 0.23 (7)	0.33 ± 0.17 (6)
	total	**58**	**61**	**57**	**58**
thumb	Ile	0.72 ± 0.20 (7)	0.72 ± 0.18 (7)	0.68 ± 0.20 (6)	0.76 ± 0.21 (7)
	Leu	0.55 ± 0.24 (11)	0.59 ± 0.29 (11)	0.55 ± 0.26 (11)	0.55 ± 0.31 (12)
	Val	0.87 ± 0.12 (9)	0.93 ± 0.16 (11)	0.84 ± 0.13 (9)	0.97 ± 0.22 (9)
	Met	0.48 (1)	0.60 (1)	none	none
	total	**28**	**30**	**26**	**28**
palm	Ile	0.87 ± 0.12 (6)	0.93 ± 0.08 (6)	0.82 ± 0.07 (6)	0.84 ± 0.27 (7)
	Leu	0.55 ± 0.29 (15)	0.63 ± 0.26 (14)	0.57 ± 0.27 (15)	0.59 ± 0.28 (14)
	Val	0.75 ± 0.29 (11)	0.82 ± 0.31 (14)	0.75 ± 0.28 (15)	0.77 ± 0.32 (12)
	Met	0.43 ± 0.18 (4)	0.44 ± 0.18 (5)	0.45 ± 0.17 (5)	0.45 ± 0.18 (5)
	total	**36**	**39**	**41**	**38**
CTD	Ile	0.57 ± 0.43 (2)	0.70 ± 0.57 (2)	0.54 ± 0.39 (2)	0.71 ± 0.59 (2)
	Leu	None	0.78 ± 0.09 (2)	0.74 ± 0.03 (2)	none
	Val	0.50 ± 0.38 (3)	0.61 ± 0.36 (4)	0.50 ± 0.36 (3)	0.51 ± 0.36 (4)
	Met	0.43 (1)	0.58 ± 0.12 (2)	0.54 ± 0.12 (2)	0.65 ± 0.19 (2)
	total	**6**	**10**	**9**	**8**
overall[a]	Ile	0.71 ± 0.24 (26)	0.75 ± 0.26 (26)	0.68 ± 0.22 (25)	0.74 ± 0.27 (27)
	Leu	0.60 ± 0.29 (51)	0.67 ± 0.28 (51)	0.61 ± 0.27 (52)	0.63 ± 0.31 (50)
	Val	0.72 ± 0.30 (45)	0.78 ± 0.31 (53)	0.70 ± 0.29 (48)	0.78 ± 0.32 (47)
	Met	0.37 ± 0.17 (12)	0.44 ± 0.20 (15)	0.42 ± 0.19 (14)	0.42 ± 0.20 (13)
	total	**134**	**145**	**139**	**137**

[a]Total for all Ile, Leu, Val, and Met residues, including those that do not belong to the canonical domains. Average values and the corresponding standard deviations are calculated over all residues of a particular type in a given structural domain.

in the rotational diffusion tensor (D_{para}/D_{perp} = 1.17). We did not expect that the neglect of this rotational anisotropy would lead to significant errors in our analyses. Therefore, assuming isotropic tumbling, the overall rotational correlation time (τ_C) for apo P2 was obtained from a 1D ^{15}N, ^1H TRACT experiment[21] measured in a buffer prepared in 90% H_2O and 10% D_2O. The difference in decay rates of the amide α-state (R_α) and β-state (R_β) envelopes yields a value of 67.8 ± 2.8 s^{-1}, corresponding to a τ_C value of 33.0 ± 1.4 ns. Using a scaling factor of 1.23 to account for the change in solvent viscosity in going from an ∼10% to an ∼100% D_2O-based buffer leads to a τ_C value of 40.6 ± 1.7 ns. Similar values (within error) were obtained for additional states of wild-type P2 and for the *ts* mutant. Thus, a τ_C value of 41 ns was used in all calculations.

To measure the dynamics of the methyl rotation axis (C_3 axis) on the picosecond to nanosecond time scale, we measured the intra-methyl $^1H-^1H$ dipole−dipole cross-correlation rate (η) (Figure 2) using the pulse sequences developed by Tugarinov et al.[17] The S_{axis}^2 values were estimated from the η and τ_C (determined above) using eq 3. A total of 134 S^2_{axis} values for the wild-type enzyme in the absence of ligands could be measured with a high degree of accuracy (Table 1). Resonances with significant spectral overlap and those with η values (average of 94.8 ± 42.6 s^{-1}; 25% trimmed mean of 101.3 ± 41.2 s^{-1}) with errors larger than 25 s^{-1} were excluded from detailed analysis. The S_{axis}^2 values in apo P2 show relatively weak correlation with simple structural features such as solvent exposure, local packing density, etc., as noted in previous studies.[29] The following overall trend is seen for P2 in the apo state: S_{axis}^2(Val, γ1/2) ∼ S_{axis}^2(Ile, δ1) > S_{axis}^2(Leu, δ1/2) > S_{axis}^2(Met, ε) (Table 1). This overall trend is maintained for the various liganded states and in the *ts* mutant discussed below.

Influence of Divalent Metal Ions on Fast Dynamics. RNA and DNA polymerases utilize divalent metal ions (Mg^{2+}) to catalyze nucleic acid polymerization.[30] MD simulations of HCV NS5B have indicated that binding of Mg^{2+} produces significant alterations in RdRp dynamics,[7] notably at regions distant from the binding site. To test this scenario for P2, η values were measured in the presence of saturating amounts of Mg^{2+}. The presence of metal ions did not elicit large-scale changes to the average structure of P2 as reflected by the absence of large chemical shift perturbations in the assigned methyl resonances. On the basis of the perturbations, the largest structural effects were found to localize to the palm domain in the conserved motifs near the metal-binding sites (note that Mg^{2+} ions occupy only noncatalytic structural sites that are displaced by ∼8 Å from the canonical catalytic sites[20] in the absence of NTPs). Residues that display significant shift perturbations (calculated using eq 4) include V350 (motif A, 0.18 ppm), I465 (motif C, 0.06 ppm), L483 (0.08 ppm), and L488 (motif D, 0.07 ppm). Some residues distant from the metal-binding site also show perturbations; the largest of these is seen for M48 (0.07 ppm).

Substantial changes in dynamics as reflected by alterations in the S_{axis}^2 values compared to that of apo P2 [ΔS_{axis}^2 is defined as S_{axis}^2(apo) − S_{axis}^2(Mg^{2+}); thus, negative values imply greater order in the presence of Mg^{2+} ions] are found in the palm domain proximal to the metal-binding site (Table S1). V434 (−0.36 ± 0.23) and I465 (−0.22 ± 0.15) of motifs B and C, respectively, display the largest overall changes in S_{axis}^2 values in the presence of Mg^{2+}. Significant ΔS_{axis}^2 values are also seen at remote sites (Figure 3, identified as those having no heavy atoms within 15 Å of any heavy atom at the binding site) at the top of the fingers domain near the template entry channel (e.g.,

DOI: 10.1021/acs.biochem.5b00828
Biochemistry 2015, 54, 5828−5838

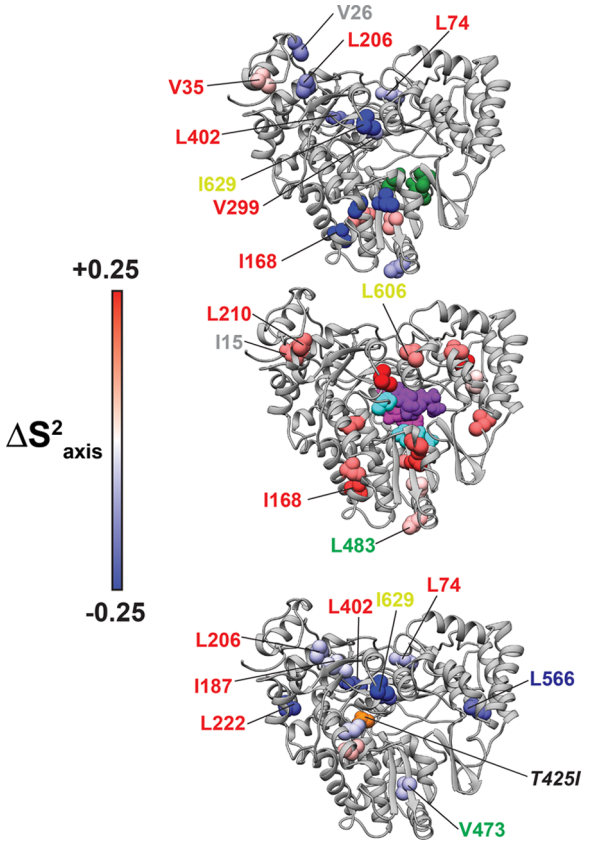

Figure 3. Residues that show statistically significant ΔS_{axis}^2 values in the presence of Mg^{2+} [compared to the unliganded state of ϕ12 P2 (top panel)], Mg^{2+}/GMPCPP [compared to the Mg^{2+}-loaded state of ϕ12 P2 (middle panel)], and for the *ts* mutant [the T425I mutant compared to the wild type, unliganded ϕ12 P2 (bottom panel)]. ΔS_{axis}^2 values between states i and j are considered to be statistically significant when $\Delta S^2_{axis} = |S^2_{axis}(i) - S^2_{axis}(j)| > \sigma S^2_{axis}(i) + \sigma S^2_{axis}(j) + 0.03$; $\sigma S^2_{axis}(i)$ is the error in the S_{axis}^2 value for the *i*th state. Remote residues (defined as those that do not have any heavy atoms within 15 Å of any other atom of the binding/mutation site) are labeled. The fonts are colored on the basis of the domain that houses a particular residue: red for fingers, green for palm, blue for thumb, and yellow for C-terminal. Residues that comprise the secondary Mg^{2+}-binding site (G348, E503, V507, and D470) are shown and colored green in the top panel. The catalytic residues (D349, D469, and D470) are colored cyan, and the two GTP molecules are colored purple and magenta in the middle panel. The site of mutation (T425I) is colored orange (and labeled in black) in the bottom panel.

L402; $\Delta S_{axis}^2 = -0.14 \pm 0.11$), the bottom of the fingers domain (e.g., I168; $\Delta S_{axis}^2 = -0.23 \pm 0.10$), and in the C-terminal domain (I629; $\Delta S_{axis}^2 = -0.22 \pm 0.13$). The experimental data support long-range coupling to the catalytic region as predicted originally by the MD simulations of Davis and Thorpe[7] on HCV NS5B and by Moustafa et al.[5] on PV 3Dpol. Interestingly, most of the statistically significant changes in S_{axis}^2 values in the presence of Mg^{2+} are less than zero (Table S1 and Figure 3), suggesting an overall decrease in flexibility. However, two of the only three residues that display significant ΔS^2_{axis} values of > 0 [V473 on motif C and M497 on motif D (Table S1)] belong to the conserved motifs that form the catalytic site. Others residues located on the conserved motifs, e.g., V434 (motif B) and I465 (motif C), showed significant ΔS_{axis}^2 values of <0 (Table S1). This could indicate a redistribution of conformational entropy within the catalytic cavity upon metal binding.

Influence of the Binding of GTP Analogues. GTP has been considered to be the initiation nucleotide in several *de novo* initiating viral RdRps, including those from bovine viral diarrhea virus (BVDV), HCV, broom mosaic virus (BMV), and, indeed, cystoviruses.[31] The reason for this could be that these viral genomes contain pyrimidine-rich 3′-ends and a purine nucleotide is required to form the correct initiation complex. However, it has been suggested that GTP could bind to the RdRp prior to transcriptional initiation acting as a mimic of the product RNA.[32] As in the case of Mg^{2+} ions described above, we investigated whether Mg^{2+}/GTP (the nonhydrolyzable analogue GMPPCP was used) could also perturb the dynamics distant from the active site. The addition of Mg^{2+}/GMPCPP resulted in no significant chemical shift perturbations compared with that with Mg^{2+} alone, and none of the resonances display $\Delta\delta$ values of >0.03 ppm, suggesting limited effects on the mean structure. However, significant changes in S_{axis}^2 values relative to that of the Mg^{2+}-bound state were seen [$\Delta S_{axis}^2 = S_{axis}^2(Mg^{2+}) - S_{axis}^2(Mg^{2+}/GMPCPP)$ (Table S1)]. Several of these are located at positions remote from the catalytic site. In fact, I168, located on the bottom of the fingers domain, showed one of the highest ΔS_{axis}^2 values (0.20 ± 0.14) [Figure 3; note that the positions of the GTP molecules in Figure 3 are modeled on their corresponding positions in the ternary complex of ϕ6 P2 with a short DNA template and two GTPs (PDB entry 1HI0);[33] it has been noted that the occupancy of NTP sites is between 1 and 2 in the absence of primer and the NTP molecules are slightly displaced from their positions in a ternary complex[34]]. Interestingly, most of the changes imply increased flexibility ($\Delta S_{axis}^2 > 0$ in most cases) in the Mg^{2+}/GMPCPP state compared to the flexibility of that with Mg^{2+} alone. In fact, overall, there are few statistically significant ΔS_{axis}^2 values, largely localized in the vicinity of the binding sites (Figure S1), when comparing the apo and Mg^{2+}/GMPCPP states. This seems to indicate that GMPCPP binding largely reverses the increased rigidity seen in P2 in the presence of Mg^{2+} alone, especially at remote locations distant from the catalytic site. That this effect is not an artifact of the removal of Mg^{2+} ions from P2 by GMPCPP is confirmed by the fact that the P2 resonances do not shift back toward their corresponding positions for the enzyme in its apo state.

Long-Range Conformational Coupling in a Functional Mutant. To further assess long-range dynamic coupling in P2, we analyzed a point mutant (T425I, on motif B). This mutant is termed a temperature-sensitive (*ts* mutant) and has an activity profile substantially different from that of the wild-type enzyme.[18] Wild-type P2 displays maximal polymerase activity at around 30 °C, while the *ts* mutant is most active around 10 °C and shows an almost linear decrease in activity at higher temperatures, becoming almost inactive at 30 °C. As seen in Figure 4A, the largest chemical shift perturbations resulting from the mutation are localized near the mutation site, though a few residues distant from it also display significant differences in chemical shift between the wild-type and *ts* mutant proteins. These include M378 (0.06 ppm) and V434 (0.04 ppm), neither of which contains any heavy atom within 10 Å of the mutation site. An analysis of the renormalized shortest path closeness scores (Π; see Materials and Methods) using both wild-type P2 and the computationally generated T425I mutant largely indicates that the residues with significant chemical shift differences ($\Delta\delta$ > 0.04 ppm) between wild-type and mutant P2

DOI: 10.1021/acs.biochem.5b00828
Biochemistry 2015, 54, 5828−5838

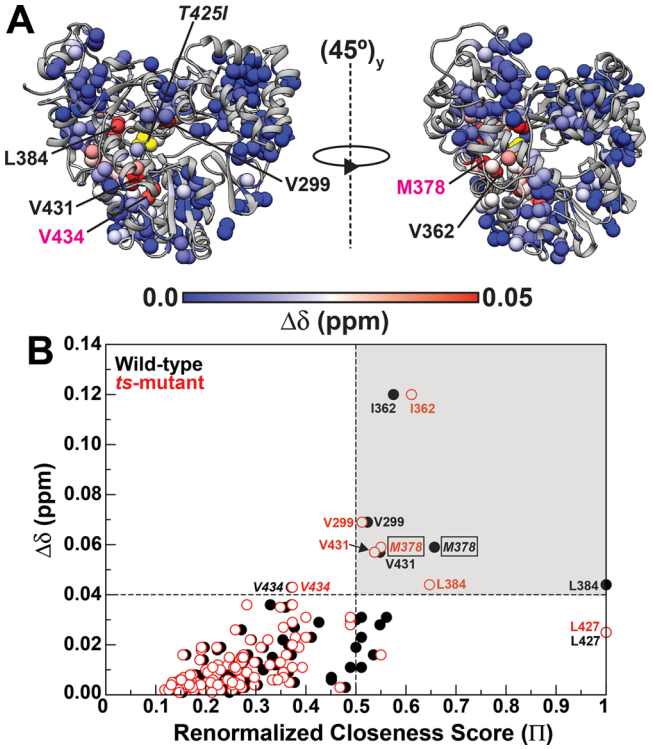

Figure 4. (A) Chemical shift differences for methyl positions between wild-type ϕ12 P2 and the *ts* mutant. Residues that display significant perturbations ($\Delta\delta$ > 0.04 ppm) are labeled. The magenta font indicates residues that do not have any heavy atoms within 10 Å of any heavy atoms of the mutation site. (B) Plot of the chemical shift changes ($\Delta\delta$) vs the renormalized closeness scores (Π) calculated using eq 5 for wild-type P2 (black circles) and the *ts* mutant (empty red circles). Residues with significant $\Delta\delta$ values (>0.04 ppm) also have large Π values (>0.5) as indicated by the shaded region in the top right quadrant bound by Π = 0.5 and $\Delta\delta$ = 0.04 ppm (indicated by the dashed lines).

proteins also display significant Π values (>0.5, the top right quadrant shaded in Figure 4B). For example, the δ1 position of I362 that has the largest difference in chemical shift ($\Delta\delta$ = 0.12 ppm) between wild-type P2 and its *ts* mutant displays Π values of 0.58 and 0.61 for the wild-type P2 and its *ts* mutant, respectively. The case of M378 (Π values of 0.66 for the wild type and 0.55 for the *ts* mutant; $\Delta\delta$ = 0.06 ppm) discussed above is quite unique in that it is relatively well networked to residue 425 in spite of not being in its immediate vicinity. However, not all residues with significant Π values also show very large $\Delta\delta$ values; this is especially true for the minimized wild-type structure (bottom right quadrant of Figure 4B). A standout example is L427 that in spite of having a Π of 1 (for both the wild type and the *ts* mutant) has a relatively modest $\Delta\delta$ of ∼0.03 ppm (Figure 4B). The overall correlation of Π and $\Delta\delta$ values is modest (Pearson correlation coefficients of 0.61 for the wild type and 0.65 for the *ts* mutant). However, one cannot expect a perfect correlation especially for side chain positions between crystallographic conformations for structures determined under cryogenic conditions with NMR data collected at room temperature. The Π and ΔS_{axis}^2 values (discussed below), not unexpectedly, are largely uncorrelated [correlation coefficients of 0.17 for the wild type and 0.24 for the *ts* mutant (data not shown)].

Compared to the chemical shift changes, long-range effects of the T425I mutation are more pronounced in the changes in dynamics between the *ts* mutant and wild-type P2 as reflected by alterations in S_{axis}^2 values. On the basis of the crystal structure of P2, we had predicted that the T425I mutation would lead to a loss of a hydrogen bonding interaction leading to increased local mobility.[20] Indeed, I425 in the mutant is highly disordered (S_{axis}^2 = 0.26 ± 0.01). However, the overall changes in dynamics suggest increased rigidity [as reflected the fact that most $\Delta S_{axis}^2 = S_{axis}^2(\text{apo}) - S_{axis}^2(ts) < 0$ (Table S1)] compared to that of the wild-type enzyme. A residue-by-residue comparison with S_{axis}^2 values in wild-type P2 reveals the expected long-range effects. Several significant ΔS_{axis}^2 values are seen for the remote residues L402 (−0.19 ± 0.14) and L222 (−0.19 ± 0.16) both from the fingers domain (Figure 3). However, the most substantial ΔS_{axis}^2 value is seen for I629 (−0.25 ± 0.21) that lies on the C-terminal domain that has no atoms within 19 Å of the site of mutation.

Anisotropic Motions. In addition to analyzing S_{axis}^2 values for P2 in the apo, Mg^{2+}-bound, and Mg^{2+}/GMPCPP-bound states and those for the *ts* mutant, we specifically compared S_{axis}^2 values for resolved γ1/γ2 and δ1/δ2 positions in Val and Leu residues, respectively. In apo P2, several residues display significant differences in the S_{axis}^2 values between their prochiral methyl positions (Table S2). In the case of L483 [$|\Delta S_{axis}^2|$ = 0.09 ± 0.03 (Table S2)], the S_{axis}^2 values are quite low (S_{axis}^2 = 0.27 ± 0.02 and 0.18 ± 0.01); the ^{13}C chemical shift difference between the prochiral positions is also small (0.64 ppm), suggesting roughly equal populations[35] of the *trans* and *gauche+* configurations and extensive averaging about the χ_2 dihedral angle. However, given the asymmetry in the S_{axis}^2 values, there appears to be additional averaging on the fast time scale independent of the averaging about χ_2. This motional axis has different projections onto the two methyl C_3 axes leading to differential effects. Anisotropic motions could explain the asymmetric S_{axis}^2 values for L427 [$|\Delta S_{axis}^2|$ = 0.16 ± 0.11 (Table S2)], though there is no significant χ_2 averaging on the fast (or perhaps any) time scale, and this is reflected in the high S_{axis}^2 values (0.91 ± 0.05 and 0.75 ± 0.06) and the significant ^{13}C chemical shift difference (3.01 ppm) between the two prochiral positions, with the latter suggesting an ∼80:20 partitioning between the two rotameric states.

The number of residues that display significant anisotropy in the S_{axis}^2 values increases to a large extent in the presence of Mg^{2+} ions. These residues include several that are remote from the Mg^{2+}-binding site, e.g., V26 ($|\Delta S_{axis}^2|$ = 0.16 ± 0.02) and V569 ($|\Delta S_{axis}^2|$ = 0.32 ± 0.07). The number of residues displaying anisotropic S_{axis}^2 values decreases substantially in the presence of GMPCPP. Thus, Mg^{2+} ions appear to induce substantial changes not only in the overall flexibility but also in the motional anisotropy as reported by the Ile, Leu, Val, and Met methyl positions of P2. While the precise details are different, profound motional effects of bivalent cations on the dynamics of viral RdRps have been noted in the MD simulations of Davis and Thorpe[7] on HCV NS5B.

Overall Flexibility on a Fast Time Scale. Another aspect borne out by the MD simulations on several homologous RdRps[5] is the differences in flexibility of individual motifs (A–F) conserved in RdRps. The presence of assigned methyl probes on every sequence motif (Table 2) allows an experimental assessment of these predictions in the case of P2. Unlike in the case of the backbone order parameters, obtaining averages over structural elements or directly comparing S_{axis}^2 values for different residue types may lead to misleading results. This is due to the fact that different atomic

DOI: 10.1021/acs.biochem.5b00828
Biochemistry 2015, 54, 5828–5838

Table 2. Σ Values for the Viral RdRp Sequence Motifs[a]

motif	ϕ12	apo	Mg^{2+}	Mg^{2+}/GMPCPP	*ts* mutant	ϕ6	apo	Mg^{2+}
F	V299, γ1/2	0.20	0.27	0.22	0.28			
F	V299, γ2/1	0.24	0.29	0.26				
A	V350, γ1/2	0.77	0.60		0.62			
A	V350, γ2/1			0.74				
B	*I425*, δ1				0.00			
B	L427, δ1/2	0.67	0.54	0.56	0.55			
B	L427, δ2/1	0.85	0.76	0.68	0.72			
B	V431, γ1/2	0.60	0.54	0.62	0.67	I408, δ1	0.72	0.75
B	V431, γ2/1		0.62	0.68				
B	V434, γ1/2		0.65	0.70	0.56			
B	V434, γ2/1	0.62	0.81	0.75	0.75			
B	I435, δ1	0.80	0.74	0.77				
C						I446, δ1	0.92	0.88
C	I465, δ1	0.48	0.64	0.65	0.68	I449, δ1	0.80	0.80
C	I472, δ1	0.64	0.71	0.62	0.78			
C	V473, γ1/2	0.14	0.09	0.06	0.17			
D	L487, δ1/2	0.13		0.17	0.24			
D	L488, δ1/2	0.16						
D	L488, δ2/1	0.10	0.12	0.07	0.22			
D	M497, ε1	0.65	0.36	0.36	0.46			
D	V500, γ1/2	0.55	0.48	0.43	0.46	I488, δ1	0.04	0.08
E						I500, δ1	0.03	0.07
E	L515, δ1/2	0.34	0.30	0.25	0.39			

[a]The corresponding residues for ϕ6 and ϕ12 P2 in the table have been aligned on the basis of their sequential position on their respective motifs (below; probe methyls are colored green). The conserved residues are shown in bold. I425 (italicized) that exists only for the *ts* mutant (T425 in the wild type) is the most dynamic of all Ile residues in the mutant.

Motif A
ϕ12: ^{349}**D**V**S**S**YD**H**S**F**S**E^{359}
ϕ6: ^{324}**D**V**S**D**HD-T**F**W**P**G^{334}
Motif B
ϕ12: ^{416}**AG**N**R**S**G**H**A**F**T**S**L**F**A**K**V**W**K**V**I**D^{436}
ϕ6: ^{393}**SG**Q**G**A**T**D**L**M**G**T**L**L**M**S**I**T**Y**L**V**M^{413}
Motif C
ϕ12: ^{461}P**F**G**C**I**N**N**GDD**E**I**V**W**F**K**S^{477}
ϕ6: ^{445}E**I**R**Q**I**S**K**SDD**A**M**L**G**W**T**K^{461}
Motif D
ϕ12: ^{487}**L**L**E**T**Q**P**Q**E**Q**R**M**F**K**V^{500}
ϕ6: ^{475}**LK**E**G**K**V**N**P**S**P**Y**M**K**I^{488}
Motif E
ϕ12: ^{505}G**A**V**FS**G**S**V**Y**Q**L**I**G^{517}
ϕ6: ^{493}G**G**A**FLGD**I**L**L**Y**D**S^{505}
Motif F
ϕ12: ^{295}**RTR**L**V**^{299}
ϕ6: ^{268}**RRRTA**^{272}

positions for the different residue types may have inherent differences in their flexibility based on the distance from the backbone and on local geometry.[29] For example, on average, the S^2_{axis} values for the Met ε position that measures the flexibility of the S−Cε bond tend to be among the lowest in proteins, while the S^2_{axis} values for the Ala β position, a measure of the flexibility of the Cα−Cβ bond, tend to be the highest.[29] To overcome this problem, we defined a parameter Σ that provides a measure of the relative mobility of a given position independent of residue type. Σ may be calculated from the measured η values using

$$\Sigma = \frac{1}{2}\left(1 + \frac{\eta - \overline{\eta_{type}}}{|\eta - \overline{\eta_{type}}|_{max}}\right) \quad (6)$$

where $\overline{\eta_{type}}$ is the η value for a particular residue type and $\left|\eta - \overline{\eta_{type}}\right|_{max}$ is the maximal deviation of an η value from the corresponding average value for that residue type (i.e., Ile, Leu, Val, or Met). Thus, Σ = 0 or Σ = 1 if a particular residue has the lowest or the highest η value, respectively, for a particular residue type. Σ = 0.5 if $\eta = \overline{\eta_{type}}$. Thus, Σ values of <0.5 suggest above average mobility. Note that even though Σ is defined for each measured η value, it is a nonlocal quantity (unlike S_{axis}^2 that is a local quantity) and represents the relative mobility of a particular methyl rotation axis compared to all others for which experimental data are available. While it is independent of global effects, e.g., changes in rotational correlation time when changing buffers, etc., it is not appropriate for use in comparing flexibilities on a residue-by-residue basis. For such cases, local quantities such as S_{axis}^2 (as

DOI: 10.1021/acs.biochem.5b00828
Biochemistry 2015, 54, 5828−5838

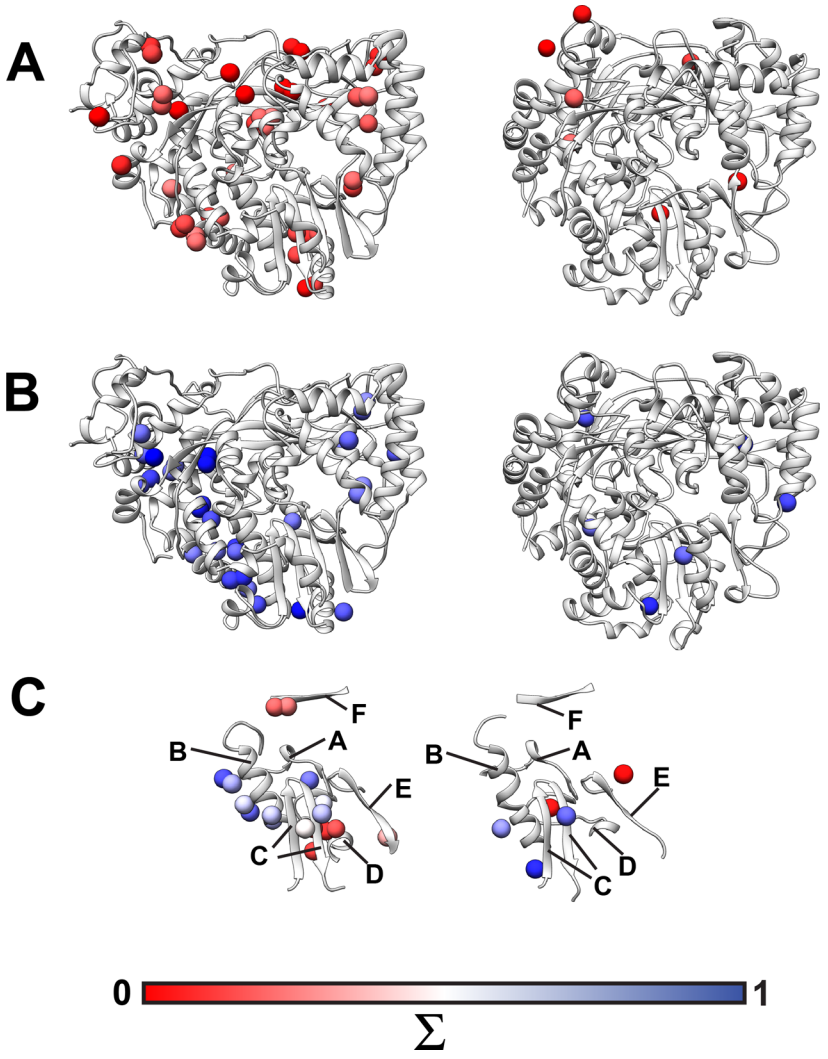

Figure 5. (A) Distribution of Σ values of ≤0.25 (calculated using eq 6) in P2. (B) Distribution of Σ values of ≥0.75. (C) Distribution of Σ values in the conserved RdRp sequence motifs (A–F) that form the catalytic site. In all cases, the P2 proteins from ϕ12 and ϕ6 cystoviruses are shown in the left and right panels, respectively.

described above) or η values themselves provide more robust measures. On the basis of the fact that ranges of S_{axis}^2 values seen in the case presented here are representative of the dynamic ranges expected in proteins, we do not suspect bias toward a particular dynamic range. Therefore, we expect that Σ values obtained here accurately represent the relative mobility even though we do not have assignments (or otherwise could not analyze the data with a sufficient level of precision) for all methyl positions for the residue types (Ile, Leu, Val, and Met) considered here.

Analysis of Σ values for the well-sampled fingers, thumb, and palm domains suggested similar distributions overall (Figure S2) with average values largely around 0.5 (Table S3; the C-terminal domain in the apo state of wild-type P2 is an exception, but this could be due to a limited number of probes), suggesting, at least for the methyl-bearing side chains analyzed here, the domains show similar fast dynamics on average. However, the lowest Σ values (≤0.25) were largely clustered around the mouth of the template entry tunnel and at the entry channel for the substrate NTPs (Figure 5A, left panel), and no positions with Σ values of ≥0.75 are seen near either entry portal (Figure 5B, left panel). Though a limited number of probes are available for ϕ6 P2 (22 of 25 and 23 of 25 Ile δ1 could be analyzed for the apo and Mg^{2+}-bound states, respectively), the overall distribution of dynamic and rigid methyl groups followed similar patterns (Figures 5A,B, right panels), suggesting that the overall pattern of fast dynamics is largely conserved at least in the cystoviral P2 proteins.

A closer inspection of the Σ values of the conserved RdRp structural motifs in P2 indicates that motifs A, B, and, to a large extent, C are well ordered while motifs D (its N-terminus is highly disordered, while its C-terminus has a higher degree of order), E, and F are more disordered, largely in line with the limited data available for ϕ6 P2 (Table 2). The spatial distribution of these residues indicates a region of order sandwiched by two regions of disorder (Figure 5C). MD simulations on several RdRps from picornaviruses suggest a substantial degree of variability in the dynamics of individual motifs; however, motifs D–F tend to be mobile in most[5] as is the case here.

Of special interest is the large degree of disorder in motif F for all states considered for ϕ12 P2 (there are no probes available for motif F in ϕ6 P2). A recent MD analysis of PV 3Dpol backed by functional studies indicates that the active site oscillates between a conformation that is incapable of binding nucleotide and another that is able to bind nucleotide. This

DOI: 10.1021/acs.biochem.5b00828
Biochemistry 2015, 54, 5828–5838

motion that involves motif F in 3Dpol purportedly contributes to the first step in nucleotide binding and takes place on the nanosecond time scale.[36] This motion then facilitates the closing of motif D that comprises the so-called fidelity checkpoint for the incorporation of the correct nucleotide occurring on a slower, millisecond time scale.[14] The nanosecond dynamics in motif F is altered in high-fidelity (G64S) and low-fidelity (H273R) mutators in 3Dpol. In our studies, motif F residue V299 (that maps onto residue I176 in 3Dpol that been shown to participate in NTP-binding occluded to NTP-binding competent transition[36]) shows significant alterations in dynamics upon the addition of Mg^{2+} (Table S1). Further changes are seen for V299 in the presence of GMPCPP (ΔS_{axis}^2 = 0.08 ± 0.06, but this change did not meet our threshold for statistical significance and is therefore not included in Table S1). Additionally, V299 in the *ts* mutant is more rigid (S_{axis}^2 = 0.52 ± 0.02) than the wild type (0.41 ± 0.03). The relationship to error incorporation in the two cases is not yet known, though the *ts* mutant does show slight differences in the relative ease of nucleotide utilization during transcription compared to that of the wild-type enzyme.[18]

CONCLUSIONS

Our studies of the ϕ12 RdRp suggest an enzyme that displays significant dynamic heterogeneity, confirming results of MD simulations on homologous systems.[5,7] The entry portals for ssRNA templates and substrate NTPs are found to be dynamic. Some catalytic motifs are found to be mostly dynamic (D−F), while others are largely rigid (A−C). The former are involved in template/NTP binding, whereas the latter are involved in metal ion binding (A and C) and in nucleotide selection (B). Cystoviral RdRps utilize single-stranded RNA templates of different sequences (albeit with different efficiencies) and various NTPs in their enzymatic reactions. A relationship between dynamics and specificity has been demonstrated before in the immunological maturation of an antibody for the T cell receptor (TCR), where higher specificity is accompanied by a reduction in the range and amplitude of fast dynamics.[37,38] It is conceivable that flexibility on the fast time scale allows the enzyme to fine-tune its interactions with templates/substrates with slightly different structural features and in doing so also helps in the efficient redistribution of conformational entropy upon binding.[39]

Additionally, remote regions appear to be dynamically coupled to the active site on the fast timescale, and perturbations at the active site through metal ion binding or point mutations lead to altered dynamics at remote regions. Indeed, several of these remote couplings cannot be fully explained by the topological analyses of static crystal structures. As mentioned earlier, MD simulations of 3Dpol have suggested long-range pathways of correlated fast dynamics.[5,9] While such detailed *in silico* results are not yet available for P2, a structure-based mapping of the 3Dpol dynamics onto P2 suggests that many of the changes in dynamics at sites remote from the region perturbed (e.g., by Mg^{2+} binding) would indeed lie on the proposed pathways (Figure S3).

While the dynamics studied here are too fast to have any direct influence on catalysis, they are likely to play a major role in determining the affinity and specificity of template or substrate binding through the influence of conformational entropy.[40] It is also possible that these motions play an indirect role in catalysis through their hierarchical influence on slower, catalytic time scales.[41] Studies of 3Dpol have suggested this hierarchical connectivity on dynamic time scales as contributing to the fidelity checkpoint in which fast dynamics in motif F (discussed above) enables the slow closure of motif D upon nucleotide binding. While we have not completed the analysis of slow (microsecond to millisecond) dynamics in P2, we do find evidence of slow dynamics in motif D as probed by multiple-quantum relaxation dispersion of the δ positions of V488 at 20 and 30 °C (Figure S4). Determining whether this is truly reflective of functional dynamics would require a full kinetic analysis of error incorporation in ϕ12 P2 as demonstrated in 3Dpol together with a complete dynamic analysis of the elongating complex.

ASSOCIATED CONTENT

Supporting Information

The Supporting Information is available free of charge on the ACS Publications website at DOI: 10.1021/acs.biochem.5b00828.

Figures S1−S4 and Tables S1−S3 described in the text and Table S4, which lists available chemical shift assignments for Ile (δ1 only), Leu, Val, and Met methyl positions in wild-type ϕ12 P2 (PDF)

AUTHOR INFORMATION

Corresponding Author

*E-mail: rghose@sci.ccny.cuny.edu.

Funding

This research has been supported by a grant from the National Science Foundation (MCB 1412007). Grant G12 MD007603 is acknowledged for partial support of the NMR facilities at The City College of New York. R.G. and S.B. are members of the New York Structural Biology Center, a NYSTAR facility.

Notes

The authors declare no competing financial interest.

ACKNOWLEDGMENTS

We thank Profs. David Boehr, Craig E. Cameron, and Ibrahim Moustafa of The Pennsylvania State University (University Park, PA) for useful discussions. We also thank Prof. Lewis Kay of the University of Toronto (Toronto, ON) for insightful discussions about methyl dynamics and for providing many of the pulse sequences used to generate data described in this work.

REFERENCES

(1) Ferrer-Orta, C., Arias, A., Escarmís, C., and Verdaguer, N. (2006) A comparison of viral RNA-dependent RNA polymerases. *Curr. Opin. Struct. Biol. 16*, 27−34.

(2) Cameron, C. E., Moustafa, I. M., and Arnold, J. J. (2009) Dynamics: the missing link between structure and function of the viral RNA-dependent RNA polymerase? *Curr. Opin. Struct. Biol. 19*, 768−774.

(3) Arnold, J. J., Vignuzzi, M., Stone, J. K., Andino, R., and Cameron, C. E. (2005) Remote site control of an active site fidelity checkpoint in a viral RNA-dependent RNA polymerase. *J. Biol. Chem. 280*, 25706−25716.

(4) Ontoria, J. M., Rydberg, E. H., Di Marco, S., Tomei, L., Attenni, B., Malancona, S., Martin Hernando, J. I., Gennari, N., Koch, U., Narjes, F., Rowley, M., Summa, V., Carroll, S. S., Olsen, D. B., De Francesco, R., Altamura, S., Migliaccio, G., and Carfí, A. (2009) Identification and biological evaluation of a series of 1H-benzo[de]-isoquinoline-1,3(2H)-diones as hepatitis C virus NS5B polymerase inhibitors. *J. Med. Chem. 52*, 5217−5227.

DOI: 10.1021/acs.biochem.5b00828
Biochemistry 2015, 54, 5828−5838

(5) Moustafa, I. M., Shen, H., Morton, B., Colina, C. M., and Cameron, C. E. (2011) Molecular dynamics simulations of viral RNA polymerases link conserved and correlated motions of functional elements to fidelity. *J. Mol. Biol. 410*, 159−181.
(6) Davis, B. C., and Thorpe, I. F. (2013) Thumb inhibitor binding eliminates functionally important dynamics in the hepatitis C virus RNA polymerase. *Proteins: Struct., Funct., Genet. 81*, 40−52.
(7) Davis, B. C., and Thorpe, I. F. (2013) Molecular simulations illuminate the role of regulatory components of the RNA polymerase from the hepatitis C virus in influencing protein structure and dynamics. *Biochemistry 52*, 4541−4552.
(8) Shen, H., Sun, H., and Li, G. (2012) What is the role of motif D in the nucleotide incorporation catalyzed by the RNA-dependent RNA polymerase from poliovirus? *PLoS Comput. Biol. 8*, e1002851.
(9) Boehr, D. D., Arnold, J. J., Moustafa, I. M., and Cameron, C. E. (2014) Structure, dynamics, and fidelity of RNA-dependent RNA polymerases. *Nucleic Acids Mol. Biol. 30*, 309−333.
(10) Boehr, D. D., Liu, X., and Yang, X. (2014) Targeting structural dynamics of the RNA-dependent RNA polymerase for anti-viral strategies. *Curr. Opin. Virol. 9*, 194−200.
(11) Ren, Z., Wang, H., and Ghose, R. (2010) Dynamics on multiple timescales in the RNA-directed RNA polymerase from the cystovirus ϕ6. *Nucleic Acids Res. 38*, 5105−5118.
(12) Ren, Z., and Ghose, R. (2011) Slow conformational dynamics in the cystoviral RNA-directed RNA polymerase P2: influence of substrate nucleotides and template RNA. *Biochemistry 50*, 1875−1884.
(13) Yang, X., Welch, J. L., Arnold, J. J., and Boehr, D. D. (2010) Long-range interaction networks in the function and fidelity of poliovirus RNA-dependent RNA polymerase studied by nuclear magnetic resonance. *Biochemistry 49*, 9361−9371.
(14) Yang, X., Smidansky, E. D., Maksimchuk, K. R., Lum, D., Welch, J. L., Arnold, J. J., Cameron, C. E., and Boehr, D. D. (2012) Motif D of viral RNA-dependent RNA polymerases determines efficiency and fidelity of nucleotide addition. *Structure 20*, 1519−1527.
(15) Liu, X., Yang, X., Lee, C. A., Moustafa, I. M., Smidansky, E. D., Lum, D., Arnold, J. J., Cameron, C. E., and Boehr, D. D. (2013) Vaccine-derived mutation in motif D of poliovirus RNA-dependent RNA polymerase lowers nucleotide incorporation fidelity. *J. Biol. Chem. 288*, 32753−32765.
(16) Alphonse, S., Arnold, J. J., Bhattacharya, S., Wang, H., Kloss, B., Cameron, C. E., and Ghose, R. (2014) Cystoviral polymerase complex protein P7 uses its acidic C-terminal tail to regulate the RNA-directed RNA polymerase P2. *J. Mol. Biol. 426*, 2580−2593.
(17) Tugarinov, V., Sprangers, R., and Kay, L. E. (2007) Probing side-chain dynamics in the proteasome by relaxation violated coherence transfer NMR spectroscopy. *J. Am. Chem. Soc. 129*, 1743−1750.
(18) Yang, H., Gottlieb, P., Wei, H., Bamford, D. H., and Makeyev, E. V. (2003) Temperature requirements for initiation of RNA-dependent RNA polymerization. *Virology 314*, 706−715.
(19) García de la Torre, J., Huertas, M. L., and Carrasco, B. (2000) HYDRONMR: prediction of NMR relaxation of globular proteins from atomic-level structures and hydrodynamic calculations. *J. Magn. Reson. 147*, 138−146.
(20) Ren, Z., Franklin, M. C., and Ghose, R. (2013) Structure of the RNA-directed RNA polymerase from the cystovirus ϕ12. *Proteins: Struct., Funct., Genet. 81*, 1479−1484.
(21) Lee, D., Hilty, C., Wider, G., and Wüthrich, K. (2006) Effective rotational correlation times of proteins from NMR relaxation interference. *J. Magn. Reson. 178*, 72−76.
(22) Delaglio, F., Grzesiek, S., Vuister, G. W., Zhu, G., Pfeifer, J., and Bax, A. (1995) NMRPipe: a multidimensional spectral processing system based on UNIX pipes. *J. Biomol. NMR 6*, 277−293.
(23) Johnson, B. A. (2004) Using NMRView to visualize and analyze the NMR spectra of macromolecules. *Methods Mol. Biol. 278*, 313−352.
(24) Boggs, P. T., Donaldson, J. R., Byrd, R. H., and Schnabel, R. B. (1989) ODRPACK software for weighted orthogonal distance regression. *ACM Trans. Math. Software 15*, 348−364.
(25) Pettersen, E. F., Goddard, T. D., Huang, C. C., Couch, G. S., Greenblatt, D. M., Meng, E. C., and Ferrin, T. E. (2004) UCSF Chimera - a visualization system for exploratory research and analysis. *J. Comput. Chem. 25*, 1605−1612.
(26) Doncheva, N. T., Klein, K., Domingues, F. S., and Albrecht, M. (2011) Analyzing and visualizing residue networks of protein structures. *Trends Biochem. Sci. 36*, 179−182.
(27) Doncheva, N. T., Assenov, Y., Domingues, F. S., and Albrecht, M. (2012) Topological analysis and interactive visualization of biological networks and protein structures. *Nat. Protoc. 7*, 670−685.
(28) Ghose, R., Fushman, D., and Cowburn, D. (2001) Determination of the rotational diffusion tensor of macromolecules in solution from NMR relaxation data with a combination of exact and approximate methods - application to the determination of interdomain orientation in multidomain proteins. *J. Magn. Reson. 149*, 204−217.
(29) Igumenova, T. I., Frederick, K. K., and Wand, A. J. (2006) Characterization of the fast dynamics of protein amino acid side chains using NMR relaxation in solution. *Chem. Rev. 106*, 1672−1699.
(30) Steitz, T. A. (1998) A mechanism for all polymerases. *Nature 391*, 231−232.
(31) van Dijk, A. A., Makeyev, E. V., and Bamford, D. H. (2004) Initiation of viral RNA-dependent RNA polymerization. *J. Gen. Virol. 85*, 1077−1093.
(32) Choi, K. H., Groarke, J. M., Young, D. C., Kuhn, R. J., Smith, J. L., Pevear, D. C., and Rossmann, M. G. (2004) The structure of the RNA-dependent RNA polymerase from bovine viral diarrhea virus establishes the role of GTP in de novo initiation. *Proc. Natl. Acad. Sci. U. S. A. 101*, 4425−4430.
(33) Butcher, S. J., Grimes, J. M., Makeyev, E. V., Bamford, D. H., and Stuart, D. I. (2001) A mechanism for initiating RNA-dependent RNA polymerization. *Nature 410*, 235−240.
(34) Wright, S., Poranen, M. M., Bamford, D. H., Stuart, D. I., and Grimes, J. M. (2012) Noncatalytic ions direct the RNA-dependent RNA polymerase of bacterial double-stranded RNA virus ϕ6 from de novo initiation to elongation. *J. Virol. 86*, 2837−2849.
(35) Hansen, D. F., Neudecker, P., Vallurupalli, P., Mulder, F. A. A., and Kay, L. E. (2010) Determination of Leu side-chain conformations in excited protein states by NMR relaxation dispersion. *J. Am. Chem. Soc. 132*, 42−43.
(36) Moustafa, I. M., Korboukh, V. K., Arnold, J. J., Smidansky, E. D., Marcotte, L. L., Gohara, D. W., Yang, X., Sanchez-Farran, M. A., Filman, D., Maranas, J. K., Boehr, D. D., Hogle, J. M., Colina, C. M., and Cameron, C. E. (2014) Structural dynamics as a contributor to error-prone replication by an RNA-dependent RNA polymerase. *J. Biol. Chem. 289*, 36229−36248.
(37) Jimenez, R., Salazar, G., Yin, J., Joo, T., and Romesberg, F. E. (2004) Protein dynamics and the immunological evolution of molecular recognition. *Proc. Natl. Acad. Sci. U. S. A. 101*, 3803−3808.
(38) Zimmermann, J., Oakman, E. L., Thorpe, I. F., Shi, X., Abbyad, P., Brooks, C. L., Boxer, S. G., and Romesberg, F. E. (2006) Antibody evolution constrains conformational heterogeneity by tailoring protein dynamics. *Proc. Natl. Acad. Sci. U. S. A. 103*, 13722−13727.
(39) Grünberg, R., Nilges, M., and Leckner, J. (2006) Flexibility and conformational entropy in protein-protein binding. *Structure 14*, 683−693.
(40) Frederick, K. K., Marlow, M. S., Valentine, K. G., and Wand, A. J. (2007) Conformational entropy in molecular recognition by proteins. *Nature 448*, 325−329.
(41) Henzler-Wildman, K. A., Lei, M., Thai, V., Kerns, S. J., Karplus, M., and Kern, D. (2007) A hierarchy of timescales in protein dynamics is linked to enzyme catalysis. *Nature 450*, 913−916.

DOI: 10.1021/acs.biochem.5b00828
Biochemistry 2015, 54, 5828−5838